System-Level Design Methodology for a Distributed Electromechanical Actuator in Bio-Inspired Robots

Bonhyun Ku and Arijit Banerjee

Department of Electrical and Computer Engineering
University of Illinois at Urbana-Champaign
Urbana, IL, USA

***Abstract*—Biological mechanisms are embraced in mobile robots to interact with their environments. Although existing biologically inspired robots perform well, their performance is limited due to the lack of a flexible spine. A vertebrate spine provides agility, a wide range of motion, balance, and efficiency. This paper proposes a system-level design methodology for a distributed and scalable actuator that mimics a robotic spine in the vertical plane. A modified limb design is introduced that significantly improves the torque capability of the distributed actuator.**

I. Introduction

The spine is one of the most important parts of vertebrates. It supports the body and allows locomotion, including agility, range of motion, motion variability [1], and balance [2]. It also allows vertebrates to be efficient [3] and natural [4]. Design principles and mechanisms from biology have been adapted to mobile and versatile robots to interact with their environment and dynamic situations [5]. Biologically inspired humanoid robots, such as "Atlas," "Valkyrie," and "DRC Hubo" have been developed [6]–[8]. Although they perform exciting maneuvers, these robots' performance do not match the natural human motions due to the lack of flexible spines.

Articulated spines have been utilized in bio-inspired robots [9]. For instance, a robot used a tendon-driven flexible spine mimicking a cheetah's spinal motion, which leads to higher energy efficiency [10]. "Charlie," a humanoid robot, improves the range of motion by 16% with its artificial spine [11]. The human mimetic humanoid robots "Kengoro" [12] and "Kenshiro" [13] are designed based on human anatomy, considering human body proportions, skeletal structure, muscle arrangement, and joint performance. They use numerous motors with tendons to mimic muscles. The spine joints provide a wide range of motion, spinal flexibility, and balancing against disturbance [14]. They also enable human-like flexible motions. One common part of these articulated spines is that they use motors for actuation. Motor rotates 360 degrees, but an actual spine's vertebra rotates only small angle. Therefore, electric motors are not optimized for the distributed actuation of a spine.

A distributed actuator for a robotic spine was presented in [15] and [16]. Series-stacked identical modules form the spine. A single module represents a vertebra, and the entire structure represents vertebrae. Each module has an E-shaped core, two coils, and two integrated step-down dc-dc converters. Each module produces torque when appropriately excited with currents. The design procedure proposed in [15] has predefined module length and height at 50 mm and 40 mm, respectively with a square-shaped core cross-sectional area. However, in practice dimensional constraints must come from the overall structure rather than the individual module.

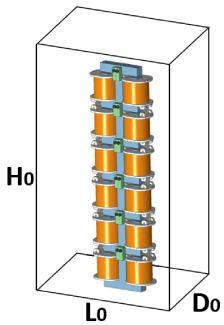

Fig. 1: A box volume $L_0 \times D_0 \times H_0$ is given for the system-level design procedure.

This paper presents a system-level design methodology for the distributed actuator that maximizes the specific torque of the overall spine. The objective is to maximize the specific torque of the entire spine for a chosen range of motion and a box-volume constraint ($L_0 \times D_0 \times H_0$), as shown in Fig. 1. The number of modules and core length are selected as design variables. Special constraints are considered to accommodate the presence of the clamps that connect two adjacent modules. Further, a limb design is introduced to improve the torque capability without compromising spine flexibility.

Section II introduces a trapezoidal limb design to improve the actuator torque capability by reducing air-gap distances between adjacent modules. Section III covers the actuator system-level design procedure with the given box-volume dimensions and range of motion. The clamp design constraints are also addressed to ensure feasible mechanical motions over the entire range. A finite element model verifies the results.

II. Trapezoidal Limb Design

The actuator's electromagnetic force can be significantly improved by modifying the limb design. Figure 2 shows the flux density distributions of the force-producing area at three

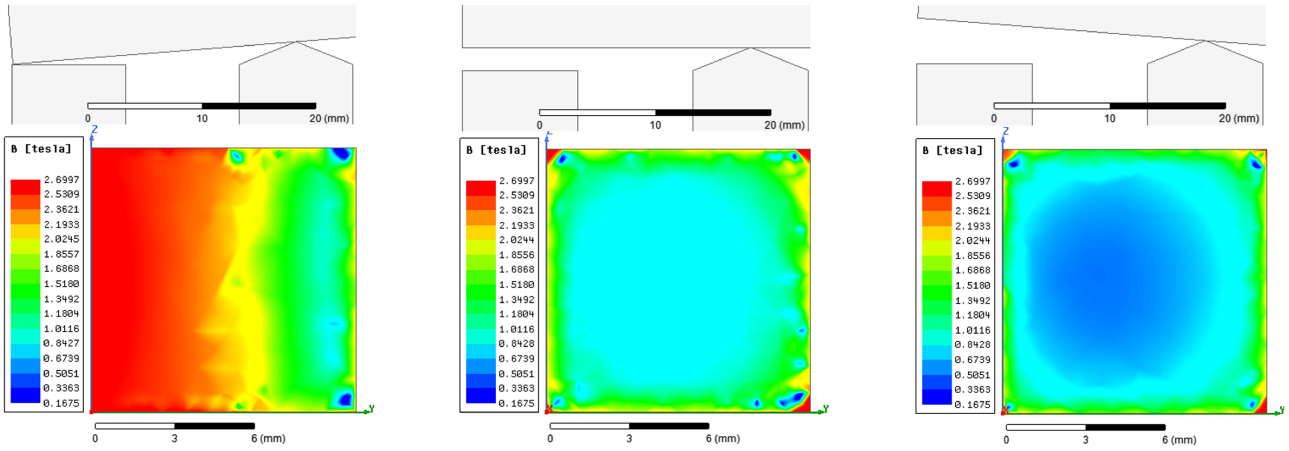

(a) 4.5 degrees (b) 0 degree (c) −4.5 degrees

Fig. 2: Flux-density distributions on the force-producing area at three different angles for the present actuator design simulated in finite element analysis (FEA). This is the previous design presented in [15].

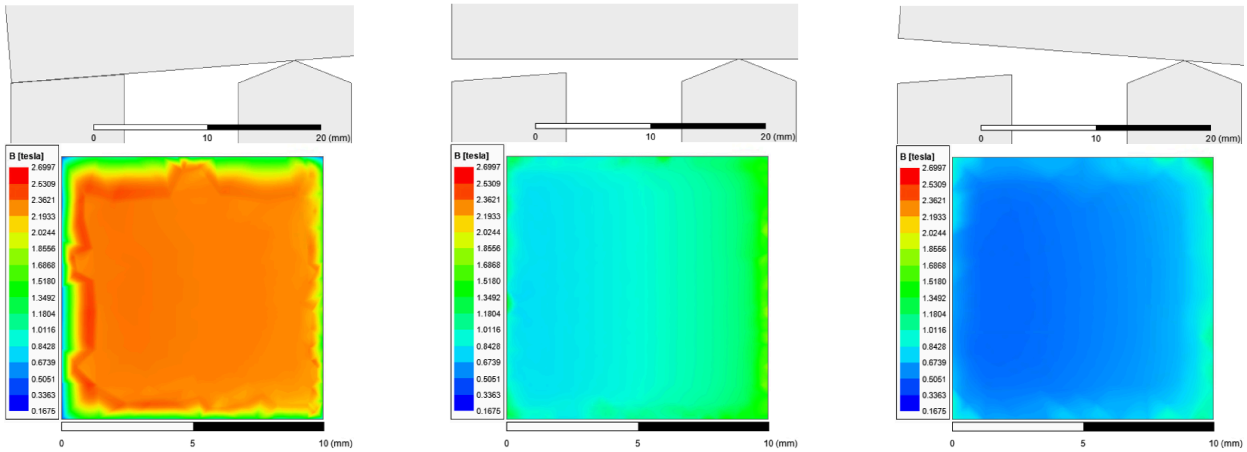

(a) 4.5 degrees (b) 0 degree (c) −4.5 degrees

Fig. 3: Proposed change in the limb design; Flux-density distributions on the force-producing area at three different angles for the modified actuator design simulated in FEA.

different angular positions with the previous actuator design in [15]. An identical 400-turn coil is excited with 3 A. The flux density is distributed at 4.5 degrees since the air gap is not uniform. At 0 degree, the air-gap distance is uniform, so the flux density is evenly distributed. At –4.5 degrees, the air-gap distance is larger; therefore, the flux density is lower over the force-producing area. At 4.5 degrees, the flux density is distributed due to the non-uniform air-gap distances over the cross-sectional area, as shown in Fig. 2(a).

The limb design is modified to a trapezoidal shape to reduce the air-gap distances at all angles, as shown in Fig. 3. Figure 3(a) shows that the upper module meets the modified limb of the lower module at the 4.5 degrees position. Hence, the air gap is zero, and the flux density is evenly high over the entire area. At 4.5 degrees position in Fig. 3(a), there is a very small gap between modules, because the actual maximum angular position is 4.58 degrees [15]. This causes fringing effect around the edges, which results in lower flux density around the boundary. When it is at the 0 degree position, the inner side of the module has higher flux density than the outer side due to the smaller air gap, as seen in Fig. 3(b). The trend is similar at the –4.5 degrees position in Fig. 3(c). With this modified design, the uniform air-gap position moved from 0 degree to 4.5 degrees.

The modified design gives the actuator much higher force capability because of the reduced air-gap distances at every angular position. Table I compares the force produced by the actuator between the current design and the modified design computed with FEA models in ANSYS Maxwell. At 4.5 degrees, the force is increased by 47.4%. Overall, the force is increased by at least 41.2%. This result indicates that the current actuator design can be significantly improved by the design change at the limb. Furthermore, the modified design can also mitigate damage to the core by spreading the force over the force-producing area, rather than applying most of it on a small section.

TABLE I: Force is significantly improved at every position by the trapezoidal limb design.

Angular position	4.5 [°]	0 [°]	−4.5 [°]
Current design	128.8 [N]	25.47 [N]	9.974 [N]
Modified design	189.8 [N]	37.04 [N]	14.08 [N]
Improvement	47.4 [%]	45.4 [%]	41.2 [%]

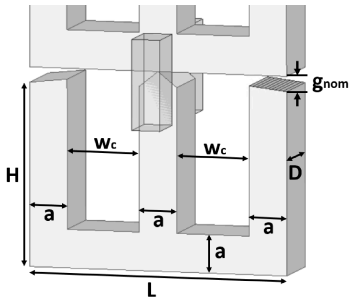

Fig. 4: Physical dimensions of a single module.

Next, an analytical model is derived that considers the trapezoidal limb to calculate the effective torque at the module level. This model will be used later on to perform system-level optimization.

Using the geometry of a single module shown in Fig. 4, the reluctance of the magnetic circuit for a module is given by

$$R(g) = \frac{g_{nom}}{\mu_0 A_c} + \frac{l_c}{\mu_0 \mu_r A_c} = \frac{1}{\mu_0 A_c}\left(g_{nom} + \frac{l_c}{\mu_r}\right), \quad (1)$$

where g_{nom} is the nominal air gap when two adjacent modules are in parallel, l_c is the average magnetic-flux-path length, μ_0 is the air permeability, μ_r is the relative core permeability, and A_c is the core cross-sectional area. Note that g_{nom} in Equation (1) will be replaced with g for non-uniform air gap analysis. Approximating the flux path to be two-dimensional, the mean length path l_c is

$$l_c = 2H + L + g_{nom} - a. \quad (2)$$

The air-gap distance is not uniform over the core cross-sectional area, as seen in Fig. 5. Approximating the wedge-shaped air gap as a uniform air gap leads to inaccuracy in the force computation. The inner edge with the smaller gap distance carries more flux and, thus, creates more force as compared to the inner edge. For instance, Figs. 3(b) and (c) show the non-uniform flux density distribution on the core surface for a coil-current excitation of 3 A. Therefore, a distributed air gap and including core saturation in the analytical model are necessary to improve the force estimation. The comparison of the force estimation using a uniform air-gap model and a distributed air-gap model was presented in [15].

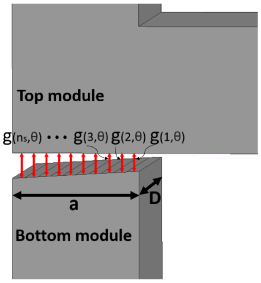

Fig. 5: The wedge-shaped air gap creates a non-uniform distance between the top and bottom cores. The angular position $\theta = 0\,^\circ$ in this case.

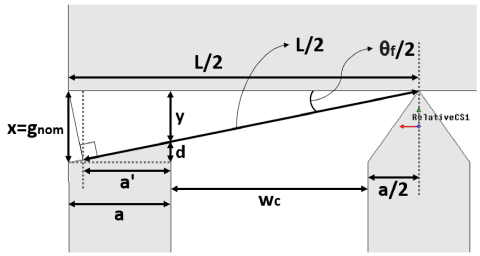

Fig. 6: The trapezoidal limb is designed to remove the gap distance between modules when fully rotated.

Figure 6 shows the derivation of the trapezoidal limb design with no air-gap distance when the module is fully rotated. The limb design allows calculation of the distributed air gaps between the two modules. When the upper module is fully rotated, the outer edges of the two modules do not exactly match, so the distance a' is given by

$$a' = \frac{L}{2}\cos\left(\frac{\theta_f}{2}\right) - \frac{a}{2} - w_c \quad (3)$$

where w_c is the coil-window width. Then the offset distance d can be calculated using ratios of the two trapezoids as

$$a' : d = \left(a' + w_c + \frac{a}{2}\right) : g_{nom} \longrightarrow d = \frac{a' \times g_{nom}}{a' + w_c + \frac{a}{2}}, \quad (4)$$

where g_{nom} is defined as the air-gap distance located at the outer edge of the core when two adjacent modules are in parallel, as seen in Fig. 6.

Two gap distances at the edges of the core are required to calculate the distributed air-gap distances. Let the distance between the outer edges of the two adjacent modules be x, and the vertical distance from the inner edge of the lower module to the upper module be y. The distances x and y are

$$\begin{cases} x = \frac{L}{2}\tan(\theta) + g_{nom} \\ y = \left(\frac{L}{2} - a\right)\tan(\theta) + g_{nom} - d. \end{cases} \quad (5)$$

The core cross-sectional area is evenly divided into n_s sections to derive the distributed air gaps. For the k^{th} section ($k = 1, 2, \cdots, n_s$), the air-gap distance at the center of each section is expressed as

$$g(k, \theta) = x + \frac{y - x}{n_s}\left(k - \frac{1}{2}\right). \quad (6)$$

The distributed air gap is dependent on the section location and the joint angle θ. The joint angle varies from $-\frac{\theta_f}{2}$ to $\frac{\theta_f}{2}$ for the distributed air-gap distance calculation.

Substituting the air-gap distance g with the distributed air gap yields the distributed reluctance as

$$R(k,\theta) = \frac{1}{\mu_0(A_c/n_s)}\left(g(k,\theta) + \frac{l_c}{\mu_r}\right). \tag{7}$$

The flux mean path length in the core l_c is assumed to be constant for simple computation, since the core reluctance is much lower than the air gaps. This approach is equivalent to constructing a parallel reluctance network model instead of a single reluctance for the air gap. For each of these distributed air gaps, the localized flux density is

$$B(k,\theta) = \frac{\mu_0 NI}{\left(g(k,\theta) + \dfrac{l_c}{\mu_r(k,\theta)}\right)}, \tag{8}$$

where N is the coil turns number, $l_c = 2H + L + g_{nom} - a$, I is the coil current, and the relative permeability $\mu_r(k,\theta)$ for each section is dependent on the coil current calculated using the B-H curve of the core material. The total force created across the gap is equal to the sum of all the forces at each section [18]:

$$f_{total} = \sum_{k=1}^{n} f(k,\theta) = \sum_{k=1}^{n} -\frac{1}{2}\frac{B(k,\theta)^2 A_c/n_s}{\mu_0}. \tag{9}$$

The equation above gives accurate force computation with an unsaturated core.

Since the force is distributed over the force producing area, each section has different moment arm length. The average moment arm length from the joint for the k^{th} section starting from the outer side of the actuator is given by

$$\begin{aligned} r(k) &= r_{out} - \frac{r_{out} - r_{in}}{n_s}\cdot k + \frac{r_{out} - r_{in}}{2n_s} \\ &= r_{out} + \frac{r_{out} - r_{in}}{n_s}\left(\frac{1}{2} - k\right) \\ &= \frac{L}{2} + \frac{a}{n_s}\left(\frac{1}{2} - k\right). \qquad (k = 1,\, 2,\, \ldots,\, n_s) \end{aligned} \tag{10}$$

This computation assumes the force is at the center of each section. The total torque is the sum of the torque from each section, which is expressed by

$$\tau_{total}(\theta) = \sum_{k=1}^{n_s} r(k) \times f(k,\theta). \tag{11}$$

The specific torque of the distributed actuator is discussed after deriving core, coil, and clamp volumes in Section III.

III. System-Level Design Procedure for Distributed Actuator with Trapezoidal Limbs

This section provides a design methodology to determine the physical dimensions of each module and the number of modules for a given box volume, as well as the spine's targeted bending angle. The design goal is to maximize specific torque at the 0 degree angular positions. Design variables are the module length L and the number of modules n. From the volume limit ($L_0 \times D_0 \times H_0$) shown in Fig. 1, the box length L_0 and height H_0 are fully used in sizing the module. The depth D_0 may not be fully utilized due to the additional clamp design constraints. Identical modules are used to form the distributed spine.

A. Design Considerations of Distributed Actuator

The angular flexibility θ_f can be expressed by the module number and the spine-bending angle. Figure 7 shows the case when all modules are fully rotated to one side to define the bending angle ϕ. The bending angle is defined as the rotated angle from the lowest module joint to the highest module joint referenced to the vertical axis. Using basic trigonometry, the relationship between bending angle and angular flexibility is approximated as

$$\tan(\phi) = \frac{\sum_{i=1}^{n-1} \sin\left(\frac{\theta_f}{2} i\right)}{\sum_{i=1}^{n-1} \cos\left(\frac{\theta_f}{2} i\right)}. \tag{12}$$

The I-shaped core is neglected, because the distance between the highest module joint to the center-of-mass position of the I-shaped core is much smaller than the regular module height. Solving the non-linear Equation (12) gives the angular flexibility of a single module θ_f. From the angular flexibility, g_{nom} is given by

$$g_{nom} = L\tan\left(\frac{\theta_f}{4}\right). \tag{13}$$

Recalling that L_0 and H_0 are fully utilized, the coil window width w_c, core limb width a, core height H, coil window height h_c and core depth D can be calculated in order as

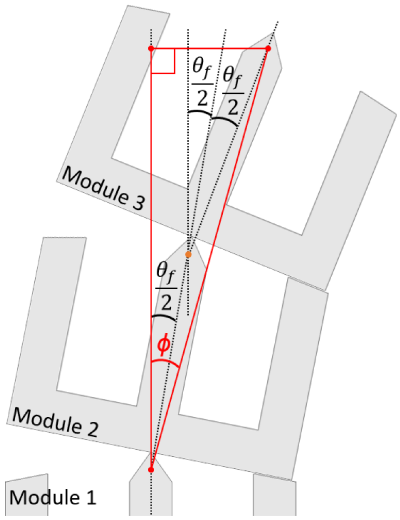

Fig. 7: The maximum bending angle ϕ occurs when all modules are fully rotated to one side.

follows:

$$\begin{cases} w_c = \dfrac{1}{2}(L_0 - L) \\ a = \dfrac{1}{3}(L - 2w_c) \\ H = \dfrac{H_0 - a}{n} - g_{nom} \\ h_c = H - a \\ D = D_0 - 2w_c. \end{cases} \tag{14}$$

However, the core depth D design in Equation (14) leads to clamp-design issues. Two clamps must be designed to provide the same cross-sectional area ($A_c = aD$) so as not to disturb flux flow through the core. Each clamp should provide half of the cross-sectional area connecting two adjacent modules. Figure 8 shows the dimensions of a clamp attached to the modules. Clamp depth d_{cl} and clamp height h_{cl} can be expressed with clamp width w_{cl} as

$$\begin{cases} d_{cl} = \dfrac{aD}{2w_{cl}} \\ h_{cl} = \dfrac{aD}{w_{cl}}. \end{cases} \tag{15}$$

The clamp width w_{cl} is the only variable in the clamp design.

Additionally, the clamp should not collide with the coils when the module rotates. Therefore, clamp design is impacted when a module is fully rotated, as seen in Fig. 9. When the clamp corner reaches the edge of the core limb, which gives design constraints, the following two equations can be obtained:

$$t\cos(\alpha) = \frac{1}{2}w_{cl}, \tag{16}$$

$$t\cos\left(\alpha - \frac{\theta_f}{2}\right) = \frac{1}{2}a, \tag{17}$$

where $t = \sqrt{(w_{cl}/2)^2 + (h_{cl}/2)^2}$. Rewriting Equation (17) above gives

$$t\cos(\alpha)\cos\left(\frac{\theta_f}{2}\right) + \left(\frac{h_{cl} - g_{nom}}{2}\right)\sin\left(\frac{\theta_f}{2}\right) = \frac{1}{2}a. \tag{18}$$

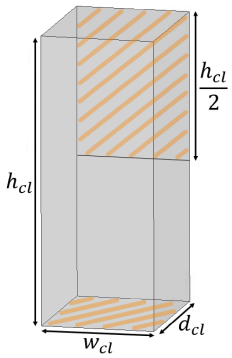

Fig. 8: Clamp dimensions ensure both shaded areas are same ($aD/2$) as half of the core cross-sectional area. Both clamps on each side keep the core cross-sectional area (aD) for the flux path.

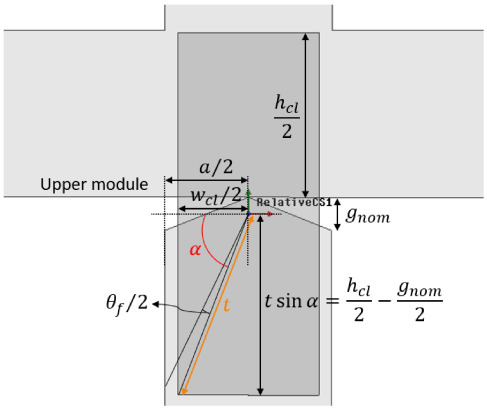

Fig. 9: The clamp should stay within the limb boundary so as not to disturb the actuator rotation.

Putting Equation (16) into (17) yields

$$\cos\left(\frac{\theta_f}{2}\right)w_{cl}^2 + \left[-a - g_{nom}\sin\left(\frac{\theta_f}{2}\right)\right]w_{cl} + aD\sin\left(\frac{\theta_f}{2}\right) = 0. \tag{19}$$

The clamp width w_{cl} is the positive solution of Equation (19) given by

$$w_{cl} = \frac{\left[a + g_{nom}\sin\left(\frac{\theta_f}{2}\right)\right]}{2\cos\left(\frac{\theta_f}{2}\right)} + \frac{\sqrt{\left[a + g_{nom}\sin\left(\frac{\theta_f}{2}\right)\right]^2 - 4aD\cos\left(\frac{\theta_f}{2}\right)\sin\left(\frac{\theta_f}{2}\right)}}{2\cos\left(\frac{\theta_f}{2}\right)}. \tag{20}$$

Moreover, the clamp upper edge should not touch the lower edge of the coils on the upper module. This creates a condition as follows:

$$\frac{h_{cl} - g_{nom}}{2} < a. \tag{21}$$

When a computed w_{cl} does not meet the condition in (21), core depth D is iteratively reduced to meet the condition, noting that $h_{cl} = \frac{aD}{w_{cl}}$.

Furthermore, the clamp lower edge should not touch the clamp upper edge on the lower module. It provides the last condition of the clamp design:

$$t < \frac{g_{nom}}{2} + H - a. \tag{22}$$

Similar to the previous process, core depth D is iteratively decreased to satisfy this condition.

The coil turns number can be determined by the coil window area and current density limit of a copper wire. The coil current density must be less than 6 A/mm^2, chosen based on natural convection cooling. The current density in the coil is given by

$$J = \frac{NI}{K_f w_s h_s} \tag{23}$$

where K_f is the coil-window fill factor. Selecting a copper

wire that has cross-sectional area A_{wire}, the coil turns number is expressed by

$$N = \frac{K_f w_s h_s}{A_{wire}}. \tag{24}$$

The specific torque can be computed using the actuator's determined dimensions. The core volume is dependent on the geometry, which is calculated as

$$V_{core} = aD(3H + L - 3a). \tag{25}$$

The clamp volume is

$$V_{clamps} = 2\, w_{cl} \cdot d_{cl} \cdot h_{cl}. \tag{26}$$

Similarly, the total volume for the two coils is given by

$$V_{coils} = 2[(L - 2a)(L - 3a + D) - aD](H - a). \tag{27}$$

Note that trapezoidal parts are ignored since they are negligibly small. Finally, the specific torque is expressed as

$$\tau_t = \frac{\tau}{\rho_{core}(V_{core} + V_{clamps}) + K_f \rho_{coils} V_{coils}}, \tag{28}$$

where ρ_{core} and ρ_{coils} are the density of the core material and copper, respectively, and V_{core} is the core volume, V_{clamps} is the clamp volume, and V_{coils} is the coil volume.

B. Design Procedure of Distributed Actuator with Trapezoidal Limbs

This section uses the analytical model defined from Section III-A and a box volume that is the torso size of the humanoid THORMANG 3. Figure 10 shows the outline for the system-level design procedure of distributed actuator. The design goal is to maximize specific torque of the spine for a selected box volume and bending angle. Based on the specifications of THORMANG 3, the box volume is chosen to be $L_0 = 160$ mm, $D_0 = 105$ mm, and $H_0 = 315$ mm [17]. The bending angle ϕ is targeted at 10 degrees. With the given box volume and bending angle, the module length L is varied between 90–110 mm, and the module number n is varied from 3 to 11. Identical modules are used for the distributed spine to make the system modular. The angular position of each module is fixed to be zero degree, which makes the spine straight. Hiperco50A, which has high saturation flux density, is used for the core material [19]. The core cross-sectional area is divided into 10 equal segments ($n_s = 10$), and the maximum flux density on each segment is limited at 1.5 T. AWG21 copper wire is used, and the coil fill factor K_f is 0.5. The coil current density remains constant at 6 A/mm^2 for natural convection heat transfer, and the turns number changes based on the design variables.

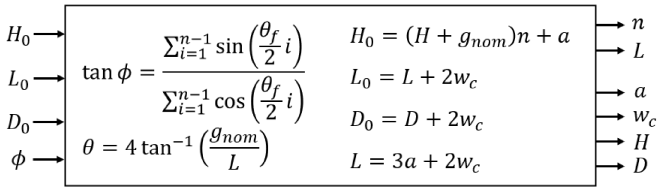

Fig. 10: With a box volume and a spine-bending angle ϕ, module dimensions are derived while varying the module number n and module length L.

Figure 11 shows that the total spine specific torque decreases when the spine bending angle increases for a fixed module number. This is because there has to be larger air-gap distances between adjacent modules for higher bending angle. Higher module number generally produces higher specific torque. However, the specific torque decreases with higher module number when bending angle is large. For example, when the bending angle is 10 degrees, the specific torque with 10 modules is greater than the one with 11 modules, as seen in Fig. 12. This is due to the coil window area reduction when the module number increases. There exists optimum module number for the specific torque at each bending angle.

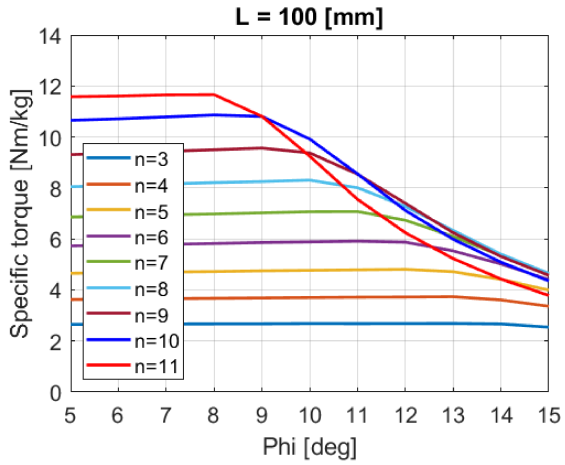

Fig. 11: Total spine specific torque decreases as the spine bending angle increases for a fixed module number.

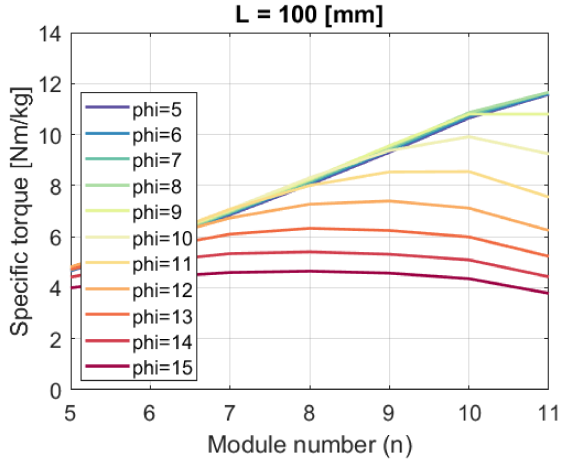

Fig. 12: Lower bending angle at a fixed module number provides higher total specific torque. Total specific torque at a fixed bending angle peaks at a module number.

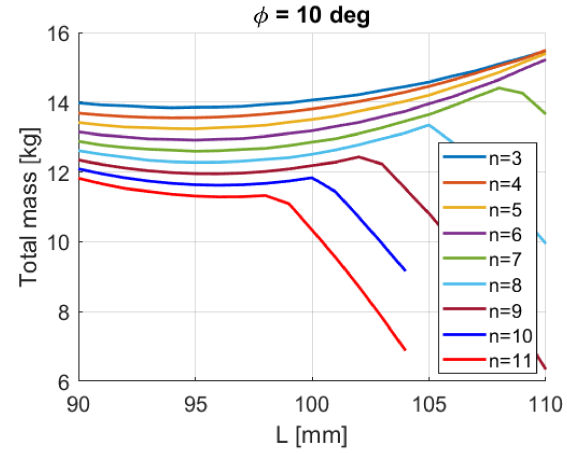

(a)

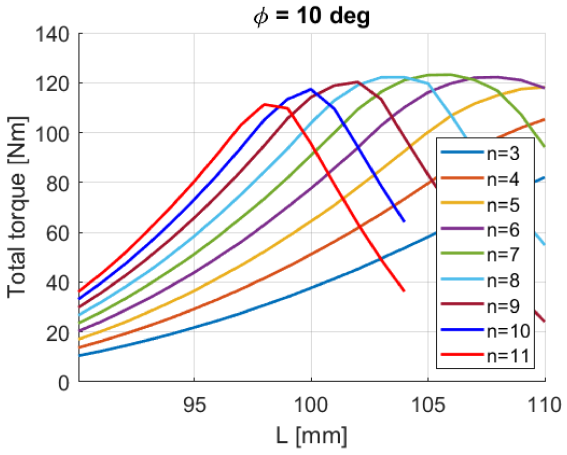

(b)

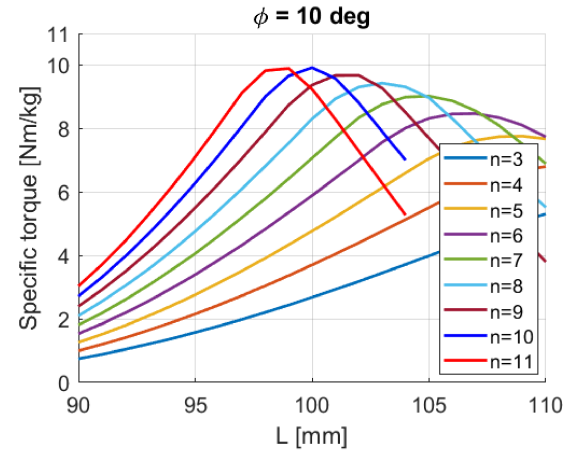

(c)

Fig. 13: At $\phi = 10\,^{\circ}$, (a) Total mass of the distributed spine (b) Total torque of the distributed spine (c) Total specific torque of the distributed spine.

Figure 13(a) displays the total mass of the entire spine at different bending angles. Total spine mass includes all clamps and an I-shaped core located on the top of the spine. There are sudden drops of the total mass when the module length is large. This is caused by the clamp-design constraints that limit the size of the core depth. The core depth must be reduced to meet the clamp-design criteria. Figure 13(b) shows the system's total torque capability considering the module numbers. The lower bending-angle case produces much higher torque because each module requires smaller air gaps for the same number of modules. For the lower module length, the higher module number case yields higher total torque, since the core is saturated at the maximum flux density. However, the total torque decreases when the core is not saturated. A large L makes the core large, and it induces a small coil size due to the L_0 constraint and the clamp-design constraints. This means that the module is not fully utilizing core flux density capability.

Specific torque of the spine is computed from the total torque and mass, as seen in Fig. 13(c). The design constraints create a maximum point for each case. A lower bending angle produces much higher specific torque. This shows the trade-off between bending angle and specific torque. At $\phi = 10$ degrees, the total specific torque peaks at 9.92 Nm/kg when the module length L is 100 mm and module number n is 10.

C. FEA Simulation Results

Figure 14 compares single module specific torque of the analytical models and FEA models when bending angle is 10 degrees and module number is 10. FEA results show that the maximum module specific torque of 10.2 Nm/kg is achieved when the module length is 101 mm. When L is large, the results match well with the analytical model. But there are relatively high mismatches when L is small. This is because the analytical model used in the design procedure does not consider core saturation and fringing effect. Strong fringing effect happens when the core cross-sectional area is small. For instance, when the module length is 90 mm, as seen in

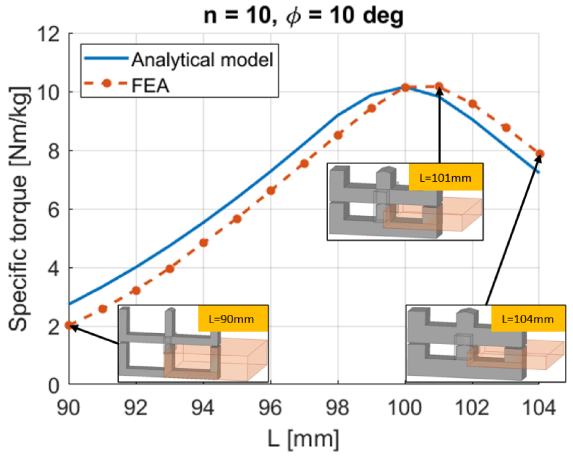

Fig. 14: Finite element analysis results show that the maximum module specific torque is 10.2 Nm/kg when module length is 101 mm.

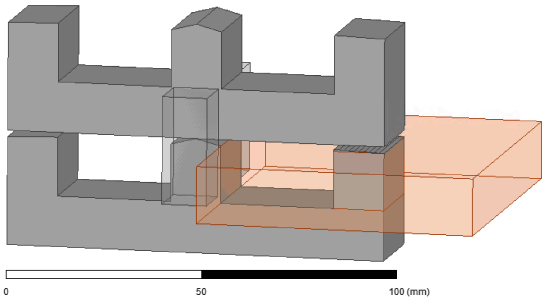

Fig. 15: Final module design yields 10.2 Nm/kg specific torque.

Fig. 14, it has small core cross-sectional area and large coil, which leads heavy core saturation and fringing effect.

Module length L = 101 mm is selected for the final design. The final module design for n = 10 and ϕ = 10 degrees is shown in Fig. 15. It gives $a = 14$ mm, $D = 24.7$ mm, $H = 28.3$ mm, and $w_c = 29.5$ mm. Each module weights 1.12 kg including E-core, two coils, and two clamps. The total mass of the spine is 11.44 kg with an I-shaped core located on the top of the spine.

Compared to the previous prototype that produces a maximum 1.42 Nm/kg at zero degree [15], the specific torque of the newly-designed distributed spine with trapezoidal limbs creates a maximum 10.2 Nm/kg specific torque and 113.4 Nm total torque at zero degree position. Although the total mass and volume are increased, the specific torque is significantly improved by the new trapezoidal limb and system-level design with fewer constraints.

IV. Conclusion

The previous module-level design of the distributed actuator had limited torque capability due to many constraints. The proposed trapezoidal limb design results in at least a 41.2 % improvement in the entire operation angles, which are verified using FEA simulations. Moreover, the proposed system-level design procedure of the distributed actuator and detailed clamp design are discussed. The design procedure is based on the given constraints, such as box-volume and bending-angle for the spine. Module dimensions are determined while varying the module number and module length. The system-level actuator design procedure with trapezoidal limb considerably increased torque and specific torque to 113.4 Nm and 10.2 Nm/kg, respectively.

Acknowledgment

This material is based upon work supported by the National Science Foundation under Grant No. 1943791. The authors would also like to thank 3M Foundation, Power Affiliates Program at the University of Illinois Urbana-Champaign, and Kwanjeong Educational Foundation for supporting this work.

References

[1] I. Mizuuchi, S. Yoshida, M. Inaba, and H. Inoue, "The development and control of a flexible-spine for a human-form robot," *Advanced Robotics*, vol. 17, no. 2, pp. 179–196, 2003.

[2] T. H. Smit, "The use of a quadruped as an in vivo model for the study of the spine - biomechanical considerations," *European Spine Journal*, vol. 11, no. 2, pp. 137–144, Apr. 2002.

[3] B. M. Haueisen, "Investigation of an articulated spine in a quadruped robotic system," PhD dissertation, University of Michigan, 2011.

[4] A. LaViers, "Make robot motions natural," *Nature*, vol. 565, pp. 422-424, 2019.

[5] N. Gravish and G. V. Lauder, "Robotics-inspired biology," *Journal of Experimental Biology*, vol. 221, no. 7, pp. 1-8, 2018.

[6] "https://www.bostondynamics.com/atlas," accessed on Dec. 12 2020.

[7] N. A. Radford, P. Strawser, K. Hambuchen, J. S. Mehling, W. K. Verdeyen, A. S. Donnan, J. Holley, J. Sanchez, V. Nguyen, L. Bridgwater, *et al.*, "Valkyrie: NASA's first bipedal humanoid robot," *Journal of Field Robotics*, vol. 32, no. 3, pp. 397–419, 2015.

[8] H. Wang, Y. F. Zheng, Y. Jun, and P. Oh, "DRC-hubo walking on rough terrains," *IEEE Int. Conf. on Technologies for Practical Robot Applications (TePRA)*, 2014.

[9] M. Haberland and S. Kim, "On extracting design principles from biology: I. Method–General answers to high-level design questions for bioinspired robots," *Bioinspir. and Biomim.*, vol. 10, no. 1, 2015.

[10] G. A. Folkertsma, S. Kim, and S. Stramigioli, "Parallel stiffness in a bounding quadruped with flexible spine," *IEEE/RSJ Int. Conf. on Intelligent Robots and Systems (IROS)*, pp. 2210-2215, 2012.

[11] D. Kuehn, A. Dettmann, and F. Kirchner, "Analysis of using an active artificial spine in a quadruped robot," *International Conference on Control, Automation, and Robotics (ICCAR)*, pp. 37–42, 2018.

[12] Y. Asano, K. Okada, and M. Inaba, "Design principles of a human mimetic humanoid: Humanoid platform to study human intelligence and internal body system," *Science Robotics*, vol. 2, no. 13, 2017.

[13] Y. Nakanishi *et al.*, "Design concept of detail musculoskeletal humanoid "Kenshiro" - Toward a real human body musculoskeletal simulator," *IEEE-RAS Int. Conf. on Humanoid Robots (Humanoids)*, pp. 1-6, 2012.

[14] Y. Asano, *et al.*, "Spine balancing strategy using muscle ZMP on musculoskeletal humanoid Kenshiro," in A. Bicchi, W. Burgard, eds., *Robotics Research, Springer Proceedings in Advanced Robotics*, vol. 2, Springer, Cham, 2018.

[15] B. Ku, Y. Tian, S. Wang, E. Libbos, S. Agrawal and A. Banerjee, "Distributed and scalable electromechanical actuator for bio-inspired robots," *IEEE Int. Electric Machines and Drives Conf. (IEMDC)*, pp. 2180-2187, 2019.

[16] B. Ku, S. Wang, and A. Banerjee, "A spring-aided two-dimensional electromechanical spine architecture for bio-inspired robots," *IEEE/RSJ Int. Conf. on Intelligent Robots and Systems (IROS)*, pp. 793-798, 2019.

[17] "https://emanual.robotis.com/docs/en/platform/thormang3/introduction/," accessed on Dec. 19 2020.

[18] N. L. Schmitz and D. W. Novotny, *Introductory Electromechanics*, Ronald Press, 1965.

[19] "https://www.edfagan.com/wp-content/uploads/2020/06/Hiperco_06_10_20.pdf," accessed on Dec. 18 2020.